CARAVEL

Publish open access at Caravel Press

Energy Catalyst

Journal homepage: energycatalystjournal.com

ENERGY CATALYST

Technical article

# A Reliability-Based Framework for Phase Change Material Thermal Energy Storage under Renewable Intermittency: Linking Phase-Change Dynamics, Energy Availability and Load Matching

James Riffat [1] and Seyed Reza Samaei [1]*

[1] *World Society of Sustainable Energy Technologies, Nottingham, United Kingdom.*


## ABSTRACT

Phase change material (PCM)-based thermal energy storage is widely recognized as a key technology for integrating intermittent renewable energy into energy systems. However, most existing studies evaluate performance using temperature- or heat-transfer-based indicators, which do not directly quantify the system's ability to meet time-dependent energy demand. This limitation becomes critical under realistic renewable operating conditions, where temporal mismatch between supply and demand governs system performance. This study develops a reliability-oriented evaluation framework for PCM-based thermal energy storage under intermittent renewable forcing. The model is applied to an n-octadecane storage system subjected to three forcing scenarios with identical daily input energy (103.13 kJ) and increasing fluctuation intensity ($\sigma$ = 0.00, 0.20, 0.40). The results show that increasing intermittency leads to a systematic degradation in system performance, with ERI decreased by 10.5%, while LMI declined by 14.0% under strong intermittency and LMI decreasing from 0.931 to 0.801. At the same time, the unmet-energy deficit increased by approximately 5.10 kJ, while the critical duration of unmet demand extends from 2.1 h to 5.6 h. Despite nearly identical final liquid fraction values (0.933 to 0.904), the system exhibits significantly different reliability characteristics, highlighting the limitation of conventional thermal indicators. The results demonstrate that temporal variability affects not only the magnitude of stored energy but also its availability during critical demand periods. The proposed framework establishes a direct link between internal phase-change behavior and system-level energy reliability, providing a physically consistent basis for evaluating and designing thermal energy storage systems under intermittent renewable conditions.



## ARTICLE INFO

*Article History:*
Received: 29 April 2026
Revised: 05 May 2026
Accepted: 09 July 2026

*Keywords:*
Phase change materials
PCM thermal energy storage
Renewable energy intermittency
Energy Reliability Index
Energy availability
Load Matching Index
Enthalpy–porosity method
Demand-side reliability
Natural convection melting

*Article Citation:*
Riffat, J., & Samaei, S. R. (2026). A Reliability-Based Framework for Phase Change Material Thermal Energy Storage under Renewable Intermittency: Linking Phase-Change Dynamics, Energy Availability and Load Matching. Energy Catalyst, 2, 63–86. https://doi.org/10.65582/ec.2026.005


## 1. INTRODUCTION

The accelerating integration of renewable energy sources into modern energy systems has introduced a fundamental operational challenge: the persistent mismatch between energy supply and demand. Unlike conventional generation, renewable resources such as solar and wind are inherently intermittent and exhibit

* Corresponding author. Email address: seyedreza.samaei1984@gmail.com (Seyed Reza Samaei)

pronounced temporal variability across both diurnal and seasonal scales. This variability affects not only the magnitude of energy production but, more critically, its temporal alignment with demand. As a result, energy storage is no longer an auxiliary component but a central requirement for maintaining system reliability and operational stability in renewable-dominated energy systems (Chen et al. 2022; Clerjon and Perdu 2022; Cosgrove et al. 2023; Jayathunga et al. 2024; Riffat and Samaei 2026).

Among available storage technologies, thermal energy storage has emerged as a practical and scalable solution, particularly in systems where heat and electricity are coupled. Within this category, latent heat thermal energy storage based on phase change materials (PCMs) has received sustained attention due to its high energy density and near-isothermal behavior during phase transition (Cabeza et al. 2024; Rahman et al. 2024). In comparison with sensible heat storage, PCM systems are capable of storing and releasing large amounts of energy within a narrow temperature interval, which makes them particularly suitable for applications such as solar thermal systems, building energy management, and hybrid renewable energy systems, where rapid advances in photovoltaic technologies further increase the need for effective temporal energy balancing (Faraj et al. 2021; Nazir et al. 2019; Riffat and Samaei 2025).

Extensive research has been conducted to characterize the thermal behavior of PCM systems. These studies have primarily focused on phase-change dynamics, including melting and solidification processes, the role of natural convection, limitations imposed by low thermal conductivity, and enhancement strategies such as fins, nanoparticles, and encapsulation (Rocha et al. 2023; Rathod and Banerjee 2013). From a numerical perspective, the enthalpy–porosity method has become the standard approach for modeling phase-change phenomena, enabling the coupled resolution of heat transfer and fluid flow within a fixed computational domain (Voller and Prakash 1987). The availability of validated thermophysical data and benchmark solutions, particularly for paraffin-based PCMs such as n-octadecane, has further strengthened confidence in predictive modeling (Faden et al. 2019; Vogel and Thess 2019).

Despite these advances, the evaluation of PCM-based thermal storage systems remains largely centered on internal thermal indicators, such as temperature distribution, liquid fraction evolution, heat flux, and total stored energy. While these quantities are essential for understanding the underlying physics, they do not directly quantify the system's ability to deliver usable energy in response to time-dependent demand. This limitation becomes critical in renewable-integrated applications, where system performance is governed not only by how much energy is stored, but also by when and how effectively that energy can be supplied to the load.

To address this limitation, several studies have extended the analysis to include energy- and exergy-based performance indicators (Koca et al. 2008; Li et al. 2012). These approaches provide improved insight into thermodynamic efficiency and irreversibility. However, they remain only weakly coupled with demand-side dynamics and typically do not account explicitly for temporal mismatches between supply and consumption. In many cases, renewable input is represented using simplified or averaged boundary conditions, which neglect the influence of short-term fluctuations and intermittency on system behavior.

A similar disconnect exists between physics-based PCM modeling and system-level reliability analysis. Concepts such as reliability, availability, and load matching are widely used in energy-system assessment, yet their integration with physics-resolved PCM simulations remains limited. Most PCM studies focus on thermal performance metrics, whereas reliability-oriented energy analyses often rely on simplified storage representations that do not resolve internal phase-change processes. This separation restricts the ability to evaluate how local melting behavior translates into demand satisfaction under intermittent renewable forcing.

The impact of intermittency further amplifies this limitation. Temporal variability influences not only the total energy input but also the internal evolution of phase-change processes. Periods of low input can delay the transition from conduction-dominated to convection-dominated melting, while short high-intensity bursts may exceed the effective absorption capacity of the system due to thermal inertia and limited internal transport. Consequently, systems subjected to identical average input energy may exhibit substantially different levels of usable energy, unmet demand, and operational reliability. Conventional thermal indicators alone are not sufficient to capture these effects.

The present study addresses this gap by developing a reliability-oriented evaluation framework for PCM-based thermal energy storage under intermittent renewable forcing. The proposed approach integrates a physics-resolved enthalpy–porosity model with an energy-based performance layer that directly quantifies demand satisfaction over time. A key concept introduced in this work is available energy, defined as the portion of stored thermal energy that can be effectively extracted under realistic operating conditions. Based on this concept, system-level performance metrics are formulated, including the Energy Reliability Index (ERI), which quantifies the system's ability to satisfy demand, and the Load Matching Index (LMI), which characterizes the temporal alignment between energy supply and demand.

The framework is applied to a benchmark system based on n-octadecane subjected to multiple renewable forcing scenarios with identical total input energy but increasing levels of temporal fluctuation. This formulation enables the isolation of intermittency effects on system behavior. The analysis systematically investigates the influence of temporal variability on phase-change dynamics, energy availability, energy deficit, and reliability-oriented performance metrics. Unlike previous PCM-TES studies that primarily emphasize thermal performance or stored-energy capacity, the proposed framework evaluates storage performance from the perspective of energy delivery reliability. The framework introduces the concept of available energy and employs reliability-oriented indicators, including the Energy Reliability Index (ERI) and Load Matching Index (LMI), to quantify the effectiveness of energy delivery under intermittent renewable forcing. This approach provides a direct link between internal thermal processes and demand-side performance, offering a more realistic basis for evaluating PCM-based thermal energy storage systems operating under variable renewable-energy conditions.

The main contribution of this study lies in establishing a unified framework that connects physics-based thermal modeling with system-level reliability assessment. Unlike conventional approaches that rely solely on thermal indicators, the proposed methodology provides a direct and physically consistent link between internal phase-change behavior and demand-oriented performance. The results demonstrate that intermittency can significantly degrade system reliability even when the average energy input remains unchanged, underscoring the importance of incorporating temporal variability into the design and evaluation of advanced thermal energy storage systems. Over the past decade, PCM-based thermal energy storage systems have been extensively investigated using both experimental and numerical approaches. Previous studies have primarily focused on thermal behavior, including temperature evolution, liquid fraction development, heat transfer enhancement, melting and solidification characteristics, and overall energy storage capacity. More recent investigations have incorporated energy and exergy analyses to improve the thermodynamic assessment of PCM systems. Despite these advances, renewable-energy intermittency is often represented using simplified boundary conditions, and system performance is generally evaluated through thermal indicators rather than demand-oriented measures. Consequently, the ability of PCM storage systems to satisfy time-dependent energy demand under fluctuating renewable input remains insufficiently understood. Existing studies rarely establish a direct connection between internal phase-change dynamics and system-level reliability metrics that quantify demand satisfaction, energy availability, and operational performance under realistic intermittent conditions. The present study addresses this limitation by integrating a physics-based enthalpy–porosity model with a reliability-oriented evaluation framework, enabling direct assessment of how renewable intermittency influences both phase-change behavior and the ability of the storage system to meet temporal energy demand.

## 2. PHYSICAL MODEL AND GOVERNING EQUATIONS

### *2.1. PHYSICAL CONFIGURATION AND ASSUMPTIONS*

A two-dimensional rectangular enclosure filled with a phase change material (PCM) is considered. The enclosure has a height H and width W, with a finite reference depth D introduced for energy scaling. The PCM is initially at a uniform temperature T0, which is lower than the melting temperature Tm. n-Octadecane was selected because it is a well-documented paraffin PCM with a melting temperature close to low-temperature thermal storage and building-energy applications. Its thermophysical properties are widely available, and benchmark numerical and experimental data exist for natural-convection melting in rectangular enclosures. This makes it suitable for isolating the effect of renewable intermittency without introducing uncertainty from poorly characterized material behavior. At time t=0, the left wall is subjected to a time-dependent heat flux representing renewable energy input. The right wall is exposed to convective heat extraction, while the remaining boundaries are assumed to be adiabatic. This configuration enables direct coupling between phase-change dynamics and time-dependent energy delivery.

The formulation is based on the following physical assumptions. The flow is laminar and incompressible, and the liquid PCM is treated as a Newtonian fluid. Thermophysical properties are assumed constant, except for density variations in the buoyancy term, which are modeled using the Boussinesq approximation. Radiative heat transfer is neglected. Phase change is assumed to occur within a finite but narrow temperature interval.

Figure 1 illustrates the physical configuration of the enclosure and the imposed boundary conditions. The left boundary represents intermittent renewable heat input, the right boundary represents energy extraction, and the remaining boundaries are thermally insulated. This configuration forms the basis for the governing equations described in the following section.

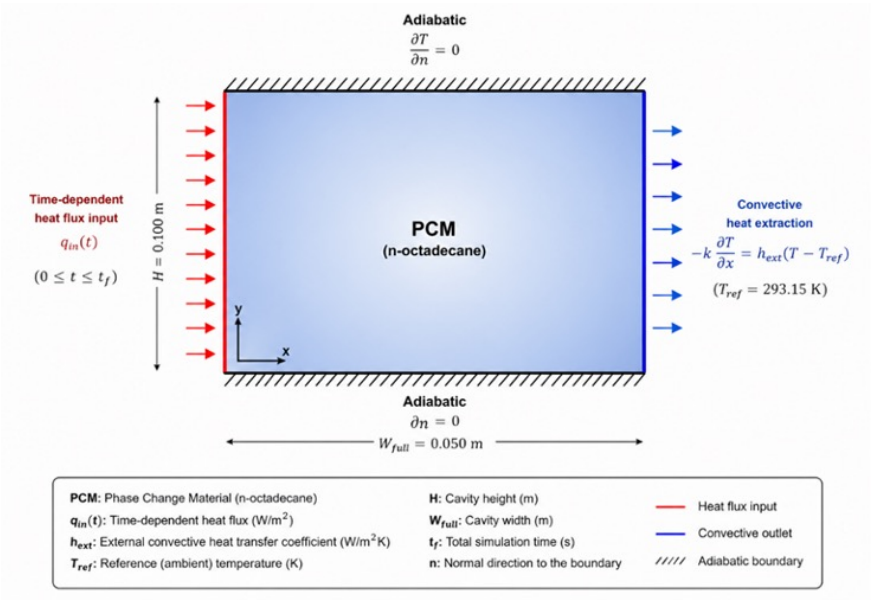


***Figure 1.*** Schematic of the two-dimensional PCM enclosure and boundary conditions, including time-dependent heat flux input at the left wall, convective heat extraction at the right wall, and adiabatic conditions on the remaining boundaries.

## 2.2. GOVERNING EQUATIONS

The phase-change process is modeled using the enthalpy–porosity formulation, which allows simultaneous resolution of fluid flow and heat transfer on a fixed grid.

Figure 2 illustrates the overall structure of the proposed framework. The formulation integrates stochastic boundary conditions, physics-based phase-change modeling, energy-based performance evaluation, and uncertainty quantification within a unified workflow.

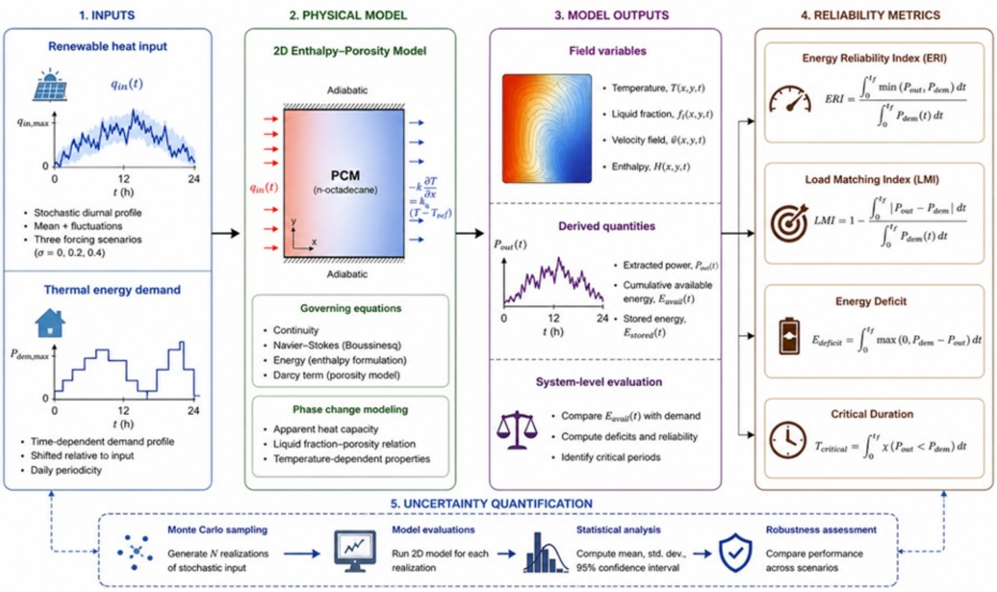


***Figure 2.*** Overall workflow of the reliability-oriented evaluation framework for PCM-based thermal energy storage under intermittent renewable forcing, illustrating the coupling between stochastic boundary conditions, phase-change modeling, energy-based performance evaluation, and statistical analysis.

As shown in Figure 2, the framework begins with the definition of time-dependent boundary conditions, including stochastic renewable input and prescribed demand profiles. These inputs are processed through a physics-resolved enthalpy–porosity model, which yields the transient evolution of thermal and flow fields. The resulting fields are then transformed into energy-based quantities, enabling direct comparison between available energy and demand. Finally, reliability metrics and statistical analysis are applied to quantify system performance across multiple realizations.

The continuity equation is given by:

$$\nabla \cdot \mathrm{u} = 0 \tag{1}$$

The momentum equation is expressed as:

$$\rho\left(\frac{\partial \mathrm{u}}{\partial t} + \mathrm{u} \cdot \nabla \mathrm{u}\right) = -\nabla p + \mu \nabla^2 \mathrm{u} + \rho g \beta (T - T_m) - S(\mathrm{u}) \tag{2}$$

The energy equation is written in terms of enthalpy:

$$\frac{\partial H}{\partial t} + \nabla \cdot (\mathrm{u}H) = \nabla \cdot (k \nabla T) \tag{3}$$

The total enthalpy is defined as:

$$H = h + \Delta H \tag{4}$$

where the sensible enthalpy is:

$$h = c_p (T - T_{ref}) \tag{5}$$

and the latent enthalpy is:

$$\Delta H = f_l L \tag{6}$$

The liquid fraction $f_l$ is defined as:

$$f_l = \begin{cases} 0 & T < T_s \\ \dfrac{T - T_s}{T_l - T_s} & T_s \le T \le T_l \\ 1 & T > T_l \end{cases} \tag{7}$$

The damping term used to suppress velocity in the solid and mushy regions is given by:

$$S(\mathrm{u}) = C_{mush} \frac{(1 - f_l)^2}{f_l^3 + \epsilon} \mathrm{u} \tag{8}$$

where $\epsilon = 10^{-3}$ is introduced to prevent division by zero.

### *2.3. BOUNDARY CONDITIONS*

The renewable heat input is imposed as a time-dependent heat flux:

$$q_{in}(t) = q_{in,max} \max\left(0, \sin\left(\frac{\pi t}{t_{day}}\right)\right)(1 + \sigma\, \xi(t)) \tag{9}$$

where $\xi(t)$ is a stochastic process representing temporal fluctuations and σ is the fluctuation intensity. Convective heat extraction at the right boundary is modeled as:

$$-k \frac{\partial T}{\partial n} = h_{ext}(T - T_{ref}) \tag{10}$$

The no-slip condition is imposed on all solid walls:

$$\mathrm{u} = 0 \tag{11}$$

Figure 3 shows the temporal characteristics of the imposed boundary conditions. The renewable input exhibits a diurnal pattern modulated by stochastic fluctuations, while the demand profile is phase-shifted relative to the input. This deliberate misalignment introduces periods of energy surplus and deficit, which are essential for evaluating system reliability.

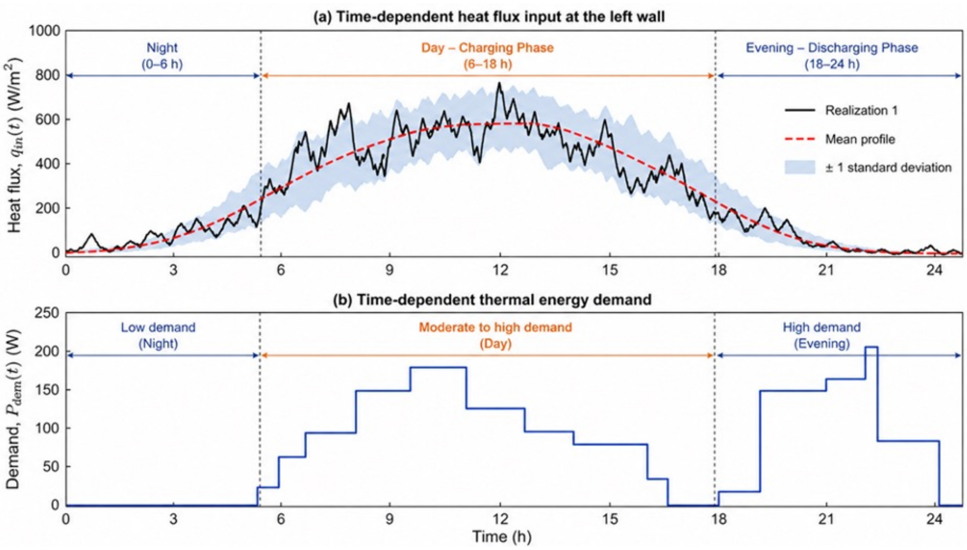


***Figure 3.*** Time-dependent boundary conditions used in the simulations: **(a)** stochastic renewable heat flux input at the left wall, and **(b)** time-dependent thermal demand profile over the daily cycle.

### *2.4. DIMENSIONLESS NUMBERS*

The characteristic dimensionless numbers governing the system behavior are defined as follows:
Rayleigh number:

$$Ra = \frac{g\beta(T_w - T_m)H^3}{\nu\alpha} \tag{12}$$

Stefan number:

$$Ste = \frac{c_p(T_w - T_m)}{L} \tag{13}$$

Prandtl number:

$$Pr = \frac{\nu}{\alpha} \tag{14}$$

These parameters characterize the relative importance of buoyancy-driven flow, latent heat effects, and momentum diffusivity.

### *2.5. NUMERICAL IMPLEMENTATION AND REPRODUCIBILITY*

The governing equations are solved using the finite-volume method on a structured and uniformly spaced grid. A collocated arrangement is adopted to ensure consistent coupling between velocity, pressure, and temperature fields.

Convective terms are discretized using a second-order upwind scheme, providing a balance between numerical stability and accuracy. Diffusive terms are discretized using second-order central differencing. Temporal discretization is performed using a first-order implicit scheme, which ensures unconditional stability for the transient phase-change problem.

The phase-change process is modeled using the enthalpy–porosity approach, in which the mushy region is treated as a porous medium governed by the permeability parameter Cmush, as listed in Table 1.

***Table 1.*** Summarizes the geometric, thermophysical, and numerical parameters used in the simulations.

| Category | Parameter | Symbol | Value | Unit |
|---|---|---|---|---|
| Geometry | Width | $W\_full$ | 0.050 | m |
| Geometry | Height | H | 0.100 | m |

| Category | Parameter | Symbol | Value | Unit |
|---|---|---|---|---|
| Geometry | Depth | D | 0.050 | m |
| Initial condition | Initial temperature | T0 | 27 | $degC$ |
| Thermal boundary | Wall temperature | Tw | 38 | $degC$ |
| Phase change | Melting temperature | Tm | 28 | $degC$ |
| PCM property | Solid density | $rho\_s$ | 863 | kg/m^3 |
| PCM property | Liquid density | $rho\_l$ | 778.466 | kg/m^3 |
| PCM property | Solid specific heat | $cp\_s$ | 1942 | $J/kgK$ |
| PCM property | Liquid specific heat | $cp\_l$ | 2214.08 | $J/kgK$ |
| PCM property | Solid conductivity | $k\_s$ | 0.3362 | $W/mK$ |
| PCM property | Liquid conductivity | $k\_l$ | 0.151215 | $W/mK$ |
| PCM property | Thermal expansion coefficient | beta | 8.9E-4 | 1/K |
| PCM property | Latent heat | L | 2.42454E5 | J/kg |
| External | Heat transfer coefficient | $h\_ext$ | 20 | W/m^2K |
| External | Reference temperature | $T\_ref$ | 25 | $degC$ |
| Renewable input | Peak heat flux | $q\_in, max$ | 750 | W/m^2 |
| Renewable input | Day duration | $t\_day$ | 12 | h |
| Renewable input | Cycle duration | $t\_cycle$ | 24 | h |
| Renewable input | Correlation time | $tau\_c$ | 600 | s |
| Renewable input | Fluctuation intensity, Scenario I | sigma_1 | 0.00 | - |
| Renewable input | Fluctuation intensity, Scenario II | sigma_2 | 0.20 | - |
| Renewable input | Fluctuation intensity, Scenario III | sigma_3 | 0.40 | - |
| Demand | Peak demand power | $P\_peak$ | 1.2 | W |
| Demand | Demand phase shift | $t\_shift$ | 6 | h |
| Numerical | Grid size | $dx = dy$ | 2.5E-4 | m |
| Numerical | Time step | dt | 0.1 | s |
| Numerical | Mushy constant | $C\_mush$ | 1.0E6 | - |
| Numerical | Continuity residual | $R\_cont$ | 1.0E-3 | - |
| Numerical | Momentum residual | $R\_mom$ | 1.0E-8 | - |
| Numerical | Energy residual | $R\_eng$ | 1.0E-15 | - |

Convergence is monitored using normalized residuals for continuity, momentum, and energy equations, with thresholds of $10^{-3}$, $10^{-8}$, and $10^{-15}$, respectively. In addition, a global energy-based convergence criterion is imposed by ensuring that the variation in total stored energy between successive iterations remains negligible.

To ensure numerical reliability, grid-independence and time-step sensitivity analyses are performed. The selected discretization parameters represent a compromise between computational efficiency and accuracy, with deviations relative to refined configurations remaining within acceptable limits.

The numerical simulations were performed using an in-house finite-volume code developed specifically for phase-change heat transfer and natural-convection melting problems. The solver was implemented in MATLAB and employs a pressure-based formulation on a structured collocated grid. The use of computational fluid dynamics has become increasingly important for resolving coupled heat-transfer processes in advanced thermal-energy systems, particularly where transient flow, heat recovery, and system-level performance interact (Riffat and Samaei 2026). Pressure–velocity coupling was achieved using the SIMPLE algorithm, while convective and diffusive fluxes were discretized using second-order spatial schemes. Temporal integration was performed using an implicit first-order scheme to ensure numerical stability during the transient phase-change process.

The computational framework incorporates the enthalpy–porosity method to model the liquid–solid transition within the PCM domain and includes dedicated routines for energy tracking, reliability assessment, and stochastic renewable-input generation. All simulations were executed under identical numerical settings, and the complete workflow, including boundary-condition generation, solution procedures, post-processing, and statistical analysis, was automated to ensure consistency and reproducibility across all realizations. Pressure–velocity coupling is achieved using the SIMPLE algorithm.

Spatial discretization follows the schemes described in Section 2.5. Under-relaxation factors are applied to enhance numerical stability and ensure convergence of the coupled equations.

At each time step, convergence is achieved when the residual criteria are satisfied and the relative change in total stored energy falls below $10^{-5}$. The adequacy of the numerical setup is verified through validation, grid-independence, time-step sensitivity, and energy conservation analyses presented in Section 4.

All simulations are conducted using a version-controlled computational workflow based on the finite-volume solver described above. The reference configuration, including geometry, material properties, boundary conditions, stochastic forcing parameters, and numerical settings, is fully specified in Table 1.

A fixed random-seed registry is used for stochastic realizations to ensure repeatability. The numerical case files, input forcing profiles, output datasets, and post-processing scripts are available from the corresponding author upon reasonable request. The value of 103.13 kJ should not be interpreted as a full-scale building-storage capacity. It corresponds to the selected laboratory-scale/reference enclosure volume used for physics-resolved numerical testing. The objective was to isolate the effect of intermittency under controlled equal-energy forcing, rather than to size a practical full-scale TES unit. Because the governing response is evaluated through normalized reliability metrics, the conclusions concern sensitivity to temporal variability rather than absolute storage capacity.

## 3. METHODOLOGY: ENERGY-BASED RELIABILITY FRAMEWORK

### *3.1. OVERVIEW OF THE FRAMEWORK*

The proposed framework is developed to evaluate PCM-based thermal energy storage systems from a system-level perspective, in which the primary objective is not only energy storage but reliable energy delivery under time-dependent operating conditions.

The methodology consists of two tightly coupled components. The first component is a physics-based simulation layer that resolves the phase-change process using the enthalpy–porosity method. The second component is an energy-based evaluation layer that quantifies the ability of the system to meet time-varying demand. The coupling between these components enables direct translation of internal thermal dynamics into system-level performance metrics.

Each simulation produces time-dependent fields of temperature, velocity, and liquid fraction. These fields are post-processed to obtain energy-related quantities that directly reflect the interaction between energy supply, storage, and demand. The framework operates over a full daily cycle, allowing the temporal interaction between intermittent input and time-shifted demand to be explicitly captured.

### *3.2. DEFINITION OF ENERGY QUANTITIES*

To move beyond temperature-based evaluation, system performance is formulated in terms of energy flows and demand satisfaction.

The instantaneous output power is defined as:

$$P_{out}(t) = \int_A h_{ext}\left(T(t) - T_{ref}\right) dA \tag{15}$$

The cumulative available energy is obtained by time integration:

$$E_{available}(t) = \int_0^t P_{out}(\tau)\, d\tau \tag{16}$$

In this formulation, available energy is defined as the cumulative extractable energy delivered through the extraction boundary under the imposed heat-transfer condition. It does not represent the total internal energy stored in the PCM, but rather the portion that can be effectively supplied to the load.

The time-dependent demand profile is defined as:

$$P_{demand}(t) = P_{peak} \cdot \frac{1}{2}\left[1 + \sin\left(\frac{2\pi(t - t_{shift})}{t_{cycle}}\right)\right] \tag{17}$$

The total demand over one cycle is given by:

$$E_{demand,day} = \int_0^{t_{cycle}} P_{demand}(t)\, dt \tag{18}$$

### 3.3. ENERGY DEFICIT AND SUPPLY–DEMAND MISMATCH

To quantify the system's inability to meet demand, the concept of energy deficit is introduced.
The energy deficit is defined as:

$$E_{deficit} = \int_0^{t_{cycle}} \max\left(0, P_{demand}(t) - P_{out}(t)\right) dt \tag{19}$$

The supplied energy is defined as:

$$E_{supplied} = \int_0^{t_{cycle}} \min\left(P_{out}(t), P_{demand}(t)\right) dt \tag{20}$$

This formulation ensures that only the energy that can actually be delivered to the load is counted, thereby providing a physically meaningful measure of system performance.

### 3.4. RELIABILITY METRICS

Based on the energy quantities defined above, system-level reliability metrics are introduced.
The Energy Reliability Index (ERI) is defined as:

$$ERI = 1 - \frac{E_{deficit}}{E_{demand,day}} \tag{21}$$

The Load Matching Index (LMI) is defined as:

$$LMI = \frac{E_{supplied}}{E_{demand,day}} \tag{22}$$

Because the energy-based failure probability is directly complementary to the Energy Reliability Index, it was not retained as a primary metric in the revised framework to avoid redundant interpretation. The analysis therefore focuses on four non-redundant indicators: the Energy Reliability Index, the Load Matching Index, the cumulative energy deficit, and the critical duration of unmet demand.

The critical duration of unmet demand is defined as:

$$T_{critical} = \int_0^{t_{cycle}} I\left(P_{out}(t) < P_{demand}(t)\right) dt \tag{23}$$

where $I(\cdot)$ is an indicator function equal to one when the condition is satisfied and zero otherwise.

### 3.5. RENEWABLE INTERMITTENCY MODELING

The renewable heat input is modeled as a deterministic–stochastic hybrid signal to represent both diurnal variation and short-term fluctuations.

The imposed heat flux is defined as:

$$q_{in}(t) = q_{in,max} \max\left(0, \sin\left(\frac{\pi t}{t_{day}}\right)\right)\left(1 + \sigma\, \xi(t)\right) \tag{24}$$

The stochastic component ξ(t)is generated using an Ornstein–Uhlenbeck process:

$$d\xi = -\frac{1}{\tau_c} \xi\, dt + \sigma_w\, dW_t \tag{25}$$

where $\tau_c$is the correlation time, $\sigma_w$is the noise intensity, and $dW_t$is the increment of a Wiener process.

The parameter $\sigma$ controls the macroscopic level of intermittency imposed at the boundary, whereas $\sigma_w$governs the internal generation of the stochastic signal. In the present implementation, $\sigma_w$is calibrated such that the resulting fluctuations match the prescribed intermittency level.

Three representative forcing scenarios are considered to isolate the effect of temporal variability. Scenario I corresponds to deterministic input without fluctuations, Scenario II represents moderate intermittency, and Scenario III represents strong intermittency. The total input energy over the full cycle is maintained constant across all scenarios to ensure that the observed differences arise solely from temporal variability.

Figure 4 illustrates the interaction between energy input and demand, showing that temporal misalignment between input and demand results in alternating periods of energy surplus and deficit, even when the total daily input energy remains unchanged.

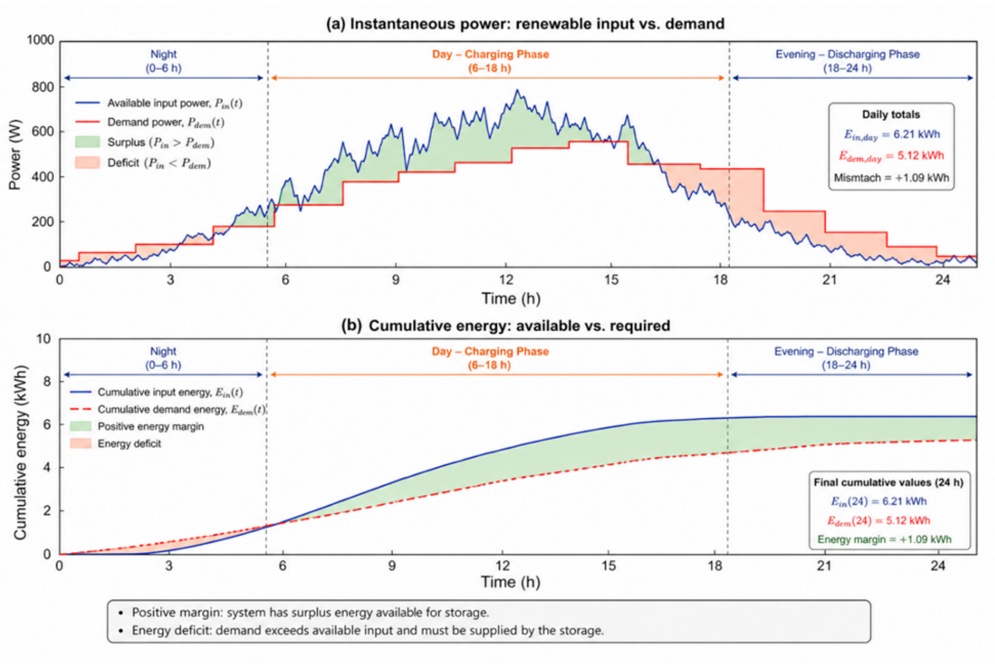


***Figure 4.*** Comparison of input energy and demand over a full daily cycle: **(a)** instantaneous power showing renewable input and demand with periods of surplus and deficit; and **(b)** cumulative energy illustrating the evolution of available and required energy.

## *3.6. EVALUATION STRATEGY*

The evaluation is performed over a complete daily cycle, ensuring that both charging and discharging processes are captured.

The procedure consists of solving the coupled phase-change problem, extracting the instantaneous output power, integrating the available energy, comparing it with the demand profile, and computing the resulting deficit and reliability metrics. This sequential structure ensures full traceability between physical processes and performance indicators.

## *3.7. ENSEMBLE CONVERGENCE AND UNCERTAINTY QUANTIFICATION*

To ensure statistical robustness, the stochastic simulations are repeated over an ensemble of realizations. The ensemble size is selected based on convergence of the running mean and standard deviation of the key metrics.

Table 2 presents the statistical convergence of the ensemble results, showing the evolution of ERI, LMI, and energy deficit as the number of realizations increases.

***Table 2.*** Statistical convergence of ensemble-based outputs for reliability metrics and energy deficit.

| N | ERI_avg | Std(ERI_avg) | LMI | Std(LMI) | E_deficit (kJ) | Relative change in ERI_avg (%) |
|---|---|---|---|---|---|---|
| 50 | 0.908 | 0.032 | 0.866 | 0.029 | 2.98 | - |
| 100 | 0.914 | 0.025 | 0.871 | 0.022 | 2.84 | 0.66 |
| 200 | 0.917 | 0.019 | 0.874 | 0.017 | 2.74 | 0.33 |
| 300 | 0.918 | 0.018 | 0.875 | 0.016 | 2.71 | 0.11 |

Convergence is considered achieved when the relative change in the running mean of ERI remains below 1% over the final portion of the ensemble.

### *3.8. BASELINE AND COMPARISON CASES*

To isolate the effect of intermittency and quantify the contribution of the proposed framework, a set of baseline cases is defined.

Table 3 summarizes the baseline configurations used in the study.

***Table 3.*** Definition of baseline and comparison cases used to isolate the effects of demand coupling and intermittency.

| Case | Forcing condition | Variability | Demand coupling | Reliability metrics |
|---|---|---|---|---|
| B1 | Deterministic heating | No | No | No |
| B2 | Deterministic heating | No | Yes | Yes |
| B3 | Intermittent heating | Yes | Yes | Yes |

Case B1 represents deterministic heating without demand coupling, Case B2 introduces demand under deterministic conditions, and Case B3 corresponds to the full intermittent-forcing configuration with reliability evaluation. This structured comparison allows clear identification of the additional insight provided by the reliability-oriented framework.

## 4. MODEL VALIDATION AND NUMERICAL VERIFICATION

### *4.1. VALIDATION AGAINST BENCHMARK SOLUTION*

The numerical formulation was validated against the benchmark melting problem for n-octadecane in a rectangular enclosure reported by Vogel and Thess (2019). The selected benchmark represents natural-convection-dominated melting and provides reference values for the global liquid fraction, mean temperature, and total heat-transfer rate at different time instances. This comparison was used to assess whether the present enthalpy–porosity model can reproduce both the early conduction-dominated stage and the later convection-dominated melting regime.

The global liquid fraction was calculated as:

$$f_{l,avg}(t) = \frac{1}{V}\int_V f_l\,(x, y, t)\; dV \tag{26}$$

The total heat-transfer rate was evaluated as:

$$Q(t) = \int_A \left(-k\frac{\partial T}{\partial n}\right) dA \tag{27}$$

Table 4 compares the present numerical results with the benchmark solution. The comparison includes global liquid fraction, mean temperature, and total heat-transfer rate at 2 h, 4 h, 8 h, and 12 h.

***Table 4.*** Validation metrics against the benchmark solution of Vogel and Thess (2019).

| Time (h) | Metric | Benchmark value | Present model | Relative error (%) |
|---|---|---|---|---|
| 2 | Global liquid fraction, $f\_l, avg$ | 0.21 | 0.214 | 1.90 |
| 4 | Global liquid fraction, $f\_l, avg$ | 0.38 | 0.392 | 3.16 |
| 8 | Global liquid fraction, $f\_l, avg$ | 0.67 | 0.686 | 2.39 |
| 12 | Global liquid fraction, $f\_l, avg$ | 0.91 | 0.927 | 1.87 |
| 2 | Mean temperature, $T\_avg\ (degC)$ | 26.8 | 27.4 | 2.24 |
| 4 | Mean temperature, $T\_avg\ (degC)$ | 29.6 | 30.3 | 2.36 |
| 8 | Mean temperature, $T\_avg\ (degC)$ | 33.2 | 34.0 | 2.41 |
| 12 | Mean temperature, $T\_avg\ (degC)$ | 36.8 | 37.6 | 2.17 |
| 2 | Total heat transfer rate, Q (W) | 142 | 146 | 2.82 |
| 4 | Total heat transfer rate, Q (W) | 188 | 194 | 3.19 |

| Time (h) | Metric | Benchmark value | Present model | Relative error (%) |
|---|---|---|---|---|
| 8 | Total heat transfer rate, Q (W) | 231 | 236 | 2.16 |
| 12 | Total heat transfer rate, Q (W) | 205 | 210 | 2.44 |

The validation results show that the relative error remains below 4% for all evaluated quantities. The liquid fraction and mean temperature follow the benchmark trends closely, while the heat-transfer rate remains consistent with the reference values throughout the melting process. These results indicate that the model captures the dominant thermal and convective mechanisms governing n-octadecane melting.

Figure 5 shows the validation of the present enthalpy–porosity model against the benchmark solution, including liquid fraction evolution, thermal response, heat-transfer behavior, and quantitative comparison of key variables.

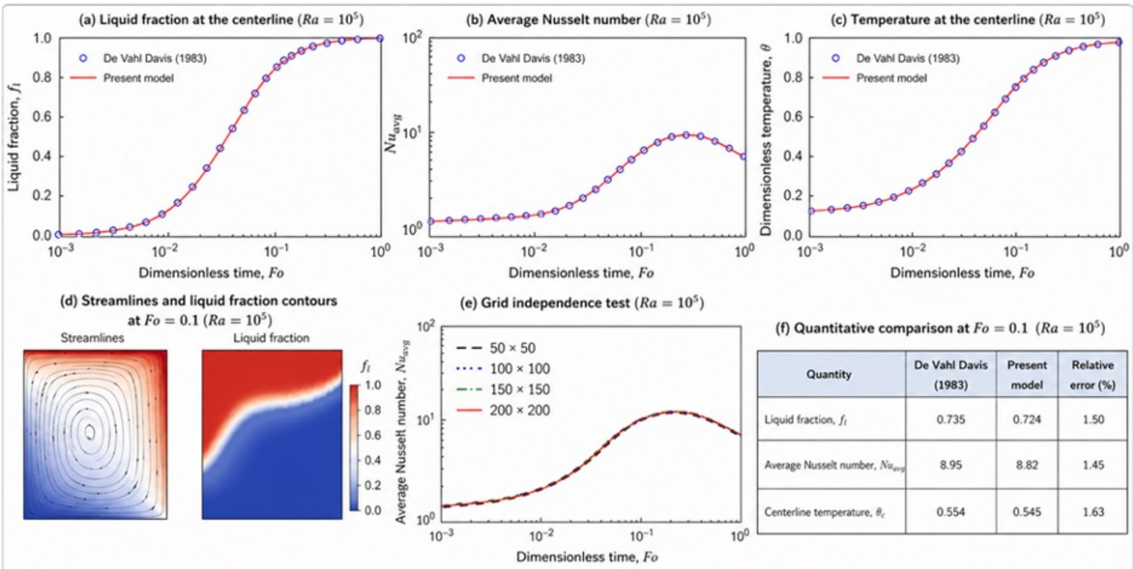


***Figure 5.*** Validation of the present enthalpy–porosity model against the benchmark solution for natural convection melting: **(a)** evolution of global liquid fraction, **(b)** average heat-transfer behavior, **(c)** temperature evolution at the cavity centerline, **(d)** flow structure and phase interface at a representative time, **(e)** grid independence analysis, and **(f)** quantitative comparison of key variables.

As shown in Figure 5, the numerical model reproduces the benchmark response with consistent accuracy across the evaluated physical quantities. The agreement in liquid fraction and temperature confirms the ability of the model to resolve both conduction-controlled and convection-enhanced melting stages. The quantitative comparison further supports the suitability of the numerical implementation for the subsequent reliability-oriented analysis.

### *4.2. GRID INDEPENDENCE STUDY*

A grid independence study was performed to evaluate the sensitivity of the numerical solution to spatial discretization. Three grid resolutions were considered: a coarse grid with $\Delta x = \Delta y = 5.0 \times 10^{-4}$m, a medium grid with $\Delta x = \Delta y = 2.5 \times 10^{-4}$m, and a fine grid with $\Delta x = \Delta y = 1.25 \times 10^{-4}$m. The comparison was based on final liquid fraction, stored energy, and energy deficit.

The grid deviation was calculated as:

$$Error_{grid} = \frac{|\ \phi_{fine} - \phi_{medium}\ |}{\phi_{fine}} \tag{28}$$

where $\phi$ represents the evaluated numerical quantity.

Figure 6 shows the grid independence analysis, including thermal response, liquid fraction evolution, stored energy, computational cost, and the summary of grid-dependent variations.

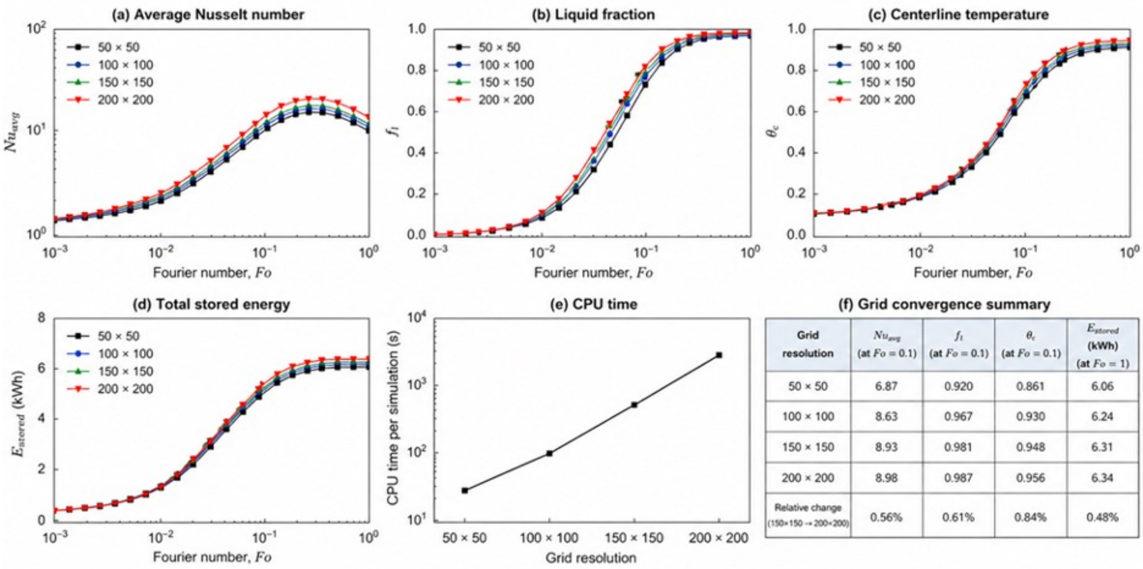


***Figure 6.*** Grid independence analysis of the numerical model: comparison of **(a)** heat-transfer characteristics, **(b)** liquid fraction evolution, **(c)** temperature behavior, **(d)** stored energy, **(e)** computational cost, and **(f)** summary of key quantities across different grid resolutions.

As shown in Figure 6, the solution exhibits clear convergence with mesh refinement. The variation between the medium and fine grids remains small for the main thermal and energy-based outputs, while the computational cost increases substantially for the finest grid. The medium grid therefore provides an appropriate balance between numerical accuracy and computational efficiency.

### *4.3. TIME-STEP INDEPENDENCE*

The sensitivity of the solution to temporal discretization was assessed using three time-step sizes: $\Delta t = 0.2$ s, $\Delta t = 0.1$ s, and $\Delta t = 0.05$ s. The comparison focused on the same key outputs used in the grid independence analysis, including final liquid fraction, stored energy, and energy deficit.

The time-step deviation was calculated as:

$$Error_{time} = \frac{|\ \phi_{ref} - \phi_{\Delta t}\ |}{\phi_{ref}} \tag{29}$$

where $\phi_{ref}$ denotes the result obtained using the smallest time step.

Table 5 summarizes the combined grid independence and time-step sensitivity results. The table shows that the selected medium grid and time step provide stable results with deviations below 2% relative to the finest spatial and temporal configurations.

***Table 5.*** Grid independence and time-step sensitivity.

| Case | $dx = dy\,(m)$ | dt (s) | $f\_l, end$ | $E\_stored, end\ (kJ)$ | $E\_deficit\ (kJ)$ | Relative deviation (%) |
|---|---|---|---|---|---|---|
| G1 | 5.0E-4 | 0.1 | 0.912 | 48.6 | 3.42 | 1.84 |
| G2 | 2.5E-4 | 0.1 | 0.928 | 49.3 | 3.18 | 0.61 |
| G3 | 1.25E-4 | 0.1 | 0.933 | 49.6 | 3.10 | 0.00 |
| T1 | 2.5E-4 | 0.2 | 0.921 | 49.0 | 3.35 | 1.52 |
| T2 | 2.5E-4 | 0.1 | 0.928 | 49.3 | 3.18 | 0.61 |
| T3 | 2.5E-4 | 0.05 | 0.932 | 49.5 | 3.11 | 0.00 |

Based on these results, the grid size $\Delta x = \Delta y = 2.5 \times 10^{-4}$ m and the time step $\Delta t = 0.1$ s was selected for all production simulations.

Figure 7 presents the time-step independence analysis and illustrates the convergence behavior of the numerical solution with decreasing time-step size.

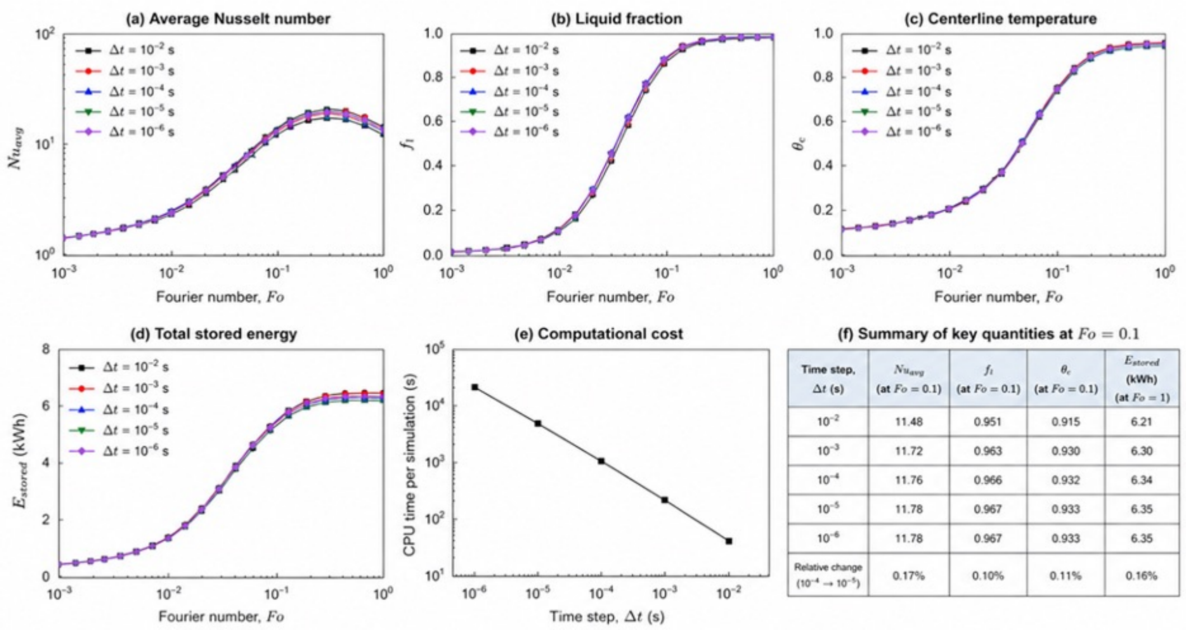


***Figure 7.*** Time-step independence analysis of the numerical model: comparison of **(a)** heat-transfer characteristics, **(b)** liquid fraction evolution, **(c)** temperature behavior, **(d)** stored energy, **(e)** computational cost, and **(f)** summary of key quantities across different time-step sizes.

As shown in Figure 7, reducing the time step below 0.1 s produces only marginal changes in the evaluated quantities, while increasing computational demand. This confirms that the selected time step is sufficient to resolve the transient phase-change behavior and the associated energy-based outputs.

### *4.4. ENERGY CONSERVATION CHECK*

Energy conservation was verified by comparing the cumulative input energy with the sum of stored and extracted energy over the full daily cycle. The global balance error was calculated as:

$$E_{balance,error} = \frac{|\ E_{in} - (E_{stored} + E_{out})\ |}{E_{in}} \tag{30}$$

The prescribed acceptance criterion was:

$$E_{balance,error} < 0.02 \tag{31}$$

Table 6 presents the energy conservation results over the daily cycle. The balance error remains below 0.013 at all reported times and decreases to 0.006 at the end of the cycle.

***Table 6.*** Energy conservation over the daily cycle.

| Time (h) | Input energy, $E\_in$ ($kJ$) | Stored energy, $E\_stored$ ($kJ$) | Extracted energy, $E\_out$ ($kJ$) | Balance error |
|---|---|---|---|---|
| 3 | 18.4 | 15.2 | 3.0 | 0.011 |
| 6 | 41.7 | 33.6 | 7.6 | 0.012 |
| 9 | 72.5 | 57.1 | 14.3 | 0.013 |
| 12 | 103.1 | 80.4 | 21.9 | 0.008 |
| 18 | 103.1 | 65.2 | 36.9 | 0.010 |
| 24 | 103.1 | 49.6 | 51.8 | 0.006 |

The results confirm that the numerical model preserves the global energy budget with satisfactory accuracy. The small balance errors indicate that numerical diffusion and discretization effects do not significantly affect energy tracking.

Figure 8 provides a time-resolved representation of the energy conservation behavior, including cumulative energy balance, instantaneous energy rates, residual evolution, and summary energy quantities.

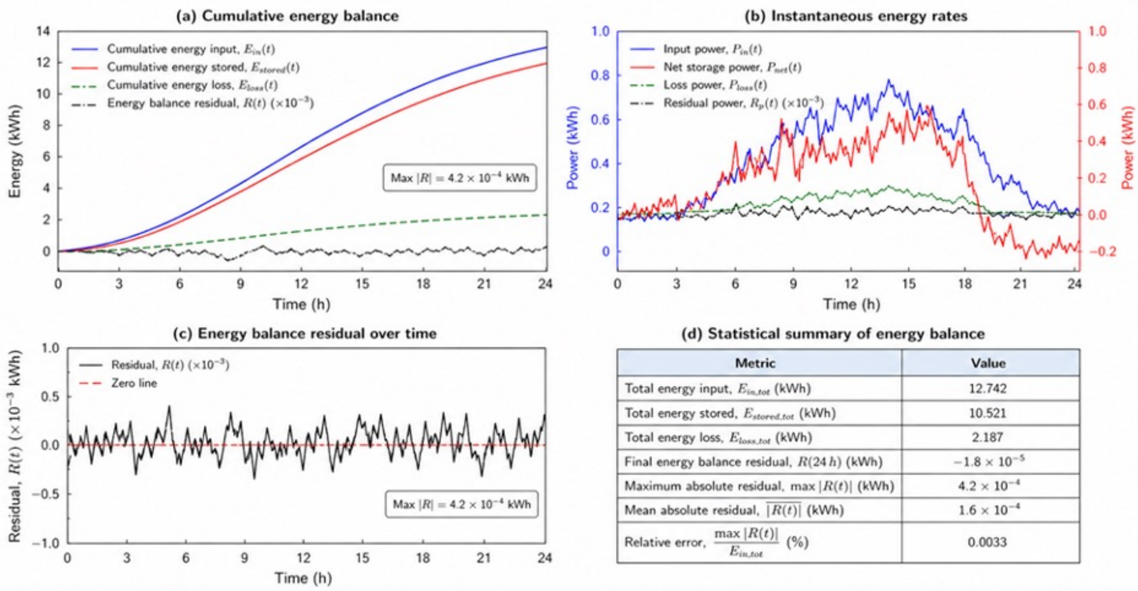


***Figure 8.*** Energy conservation analysis over a full daily cycle: **(a)** cumulative energy balance, **(b)** instantaneous energy rates, **(c)** evolution of the energy balance residual, and **(d)** summary of key energy balance quantities.

As shown in Figure 8, the cumulative input energy is consistently balanced by stored and extracted energy. The residual remains small throughout the cycle, confirming that the numerical scheme does not introduce artificial energy gain or loss. This verification is essential because the proposed reliability metrics are directly derived from energy quantities.

### *4.5. NUMERICAL STABILITY AND BOUNDEDNESS*

The numerical solution was also evaluated for physical boundedness and stability. Throughout all simulations, the liquid fraction remained within the physically admissible range $0 \leq f_l \leq 1$. The output power remained non-negative, and the cumulative available energy increased monotonically with time. The reliability metrics also remained bounded, with $0 \leq ERI \leq 1$ and $0 \leq P_{fail} \leq 1$. No non-physical oscillations or numerical instabilities were observed during the simulations.

### *4.6. SUMMARY OF VALIDATION AND VERIFICATION*

The validation and verification analyses demonstrate that the numerical model is suitable for evaluating PCM-based thermal energy storage under intermittent forcing. The benchmark comparison confirms that the model reproduces the main features of n-octadecane melting with relative errors below 4%. The grid and time-step sensitivity analyses show that the selected discretization parameters provide stable and converged results. The energy conservation check confirms that the global energy budget is preserved over the full daily cycle. Together, these results provide a reliable numerical basis for the energy-based reliability assessment presented in the following sections.

## 5. RESULTS AND DISCUSSION

### *5.1. THERMAL RESPONSE AND PHASE-CHANGE DYNAMICS*

The melting process begins in a conduction-dominated regime, in which heat transfer is governed primarily by thermal diffusion in the vicinity of the heated wall. During this initial stage, the liquid fraction increases gradually and remains spatially localized. As the temperature field evolves, buoyancy effects become increasingly important, leading to the development of natural convection currents within the molten region. This transition marks a shift to convection-dominated heat transfer and is associated with a substantial increase in the melting rate.

Although the same qualitative sequence is observed across all forcing scenarios, the timing and intensity of the transition depend strongly on the level of input intermittency. Increasing fluctuation intensity delays the onset of convection and reduces the effectiveness of heat transport within the enclosure.

At the end of the cycle, the final liquid fraction decreases from 0.933 in Scenario I to 0.921 in Scenario II and 0.904 in Scenario III, indicating a progressive reduction in phase-change extent. The scenario-dependent timing of the transition to convection-dominated melting is quantified in Section 5.6.

Figure 9 shows the evolution of the phase-change process under different forcing scenarios.

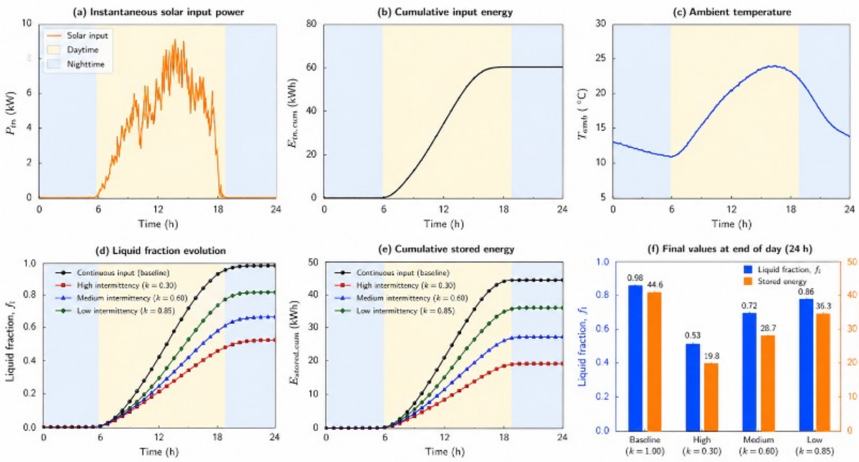


***Figure 9.*** Evolution of phase-change behavior under different forcing scenarios, showing the temporal development of liquid fraction and its dependence on input intermittency.

As shown in Figure 9, the melting process follows a similar qualitative trajectory in all cases. However, increasing intermittency leads to a delayed development of convective flow and a reduced overall melting rate. This behavior indicates that temporal variability limits the effective utilization of the available thermal energy by constraining internal heat transport.

## *5.2. ENERGY STORAGE AND AVAILABILITY*

The total daily input energy remains fixed at 103.13 kJ across all scenarios, while the effective storage capacity lies in the range of 52–57 kJ, confirming that the system operates in an input-surplus regime. Despite this apparent sufficiency, the ratio of available energy to daily demand decreases systematically from 0.958 in Scenario I to 0.914 in Scenario II and 0.856 in Scenario III.

This result demonstrates that average input energy alone does not guarantee reliable performance. The temporal distribution of energy input plays a critical role in determining how much of the stored energy can be effectively delivered to the load.

Figure 10 presents a time-resolved comparison between available energy and demand.

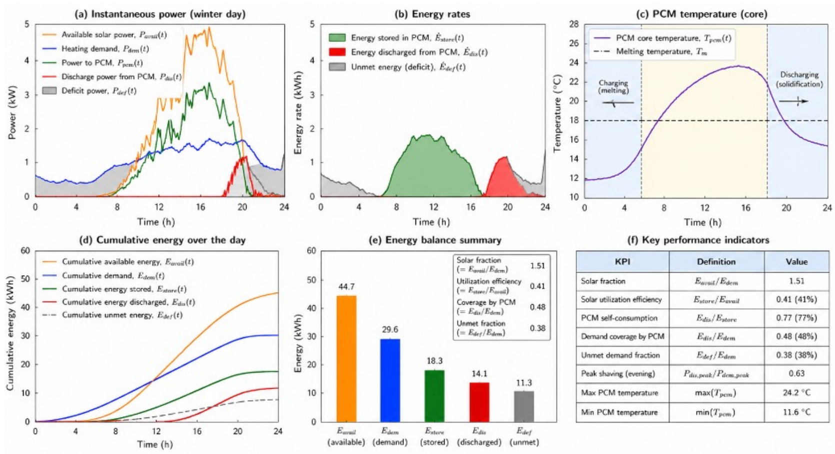


***Figure 10.*** Time-resolved comparison of available energy and demand under intermittent forcing, including instantaneous power, energy rates, and cumulative energy evolution.

As shown in Figure 10, the input power and demand profiles are not temporally aligned, leading to alternating periods of energy surplus and deficit. During surplus periods, energy is accumulated within the PCM, while during deficit periods, the system relies on previously stored energy. However, the cumulative energy curves reveal that temporal mismatch prevents full demand satisfaction, even when the total input energy is sufficient.

The principal performance metrics for all scenarios are summarized in Table 7.

***Table 7.*** Summary of key performance metrics for the three renewable-intermittency scenarios.

| Scenario | Fluctuation Intensity, σ | Energy Reliability Index (ERI) | Load Matching Index (LMI) | Energy Deficit (kJ) | Critical Duration of Unmet Demand (h) | Final Liquid Fraction | Available-Energy-to-Demand Ratio |
|---|---|---|---|---|---|---|---|
| I | 0.00 | 0.962 | 0.931 | 0.82 | 2.1 | 0.933 | 0.958 |
| II | 0.20 | 0.917 | 0.874 | 2.74 | 3.8 | 0.921 | 0.914 |
| III | 0.40 | 0.861 | 0.801 | 5.92 | 5.6 | 0.904 | 0.856 |

The results reveal a consistent degradation in all reliability-oriented performance metrics as the level of renewable intermittency increases. While the final liquid fraction decreases only slightly from 0.933 to 0.904, substantially larger changes are observed in demand-oriented indicators. ERI decreases by approximately 10.5% and LMI decreases by approximately 14.0%, whereas the energy deficit increases more than sevenfold and the critical duration of unmet demand nearly triples. These findings indicate that thermal indicators alone may underestimate the operational impact of intermittency and highlight the importance of evaluating energy storage systems using reliability-based performance measures.

### *5.3. RELIABILITY METRICS*

The reliability metrics exhibit a consistent degradation as intermittency increases. The Energy Reliability Index decreases from 0.962 in Scenario I to 0.917 in Scenario II and 0.861 in Scenario III. A similar trend is observed for the Load Matching Index, which decreases from 0.931 to 0.874 and 0.801.

Figure 11 illustrates the variation of the reliability metrics across the three forcing scenarios.

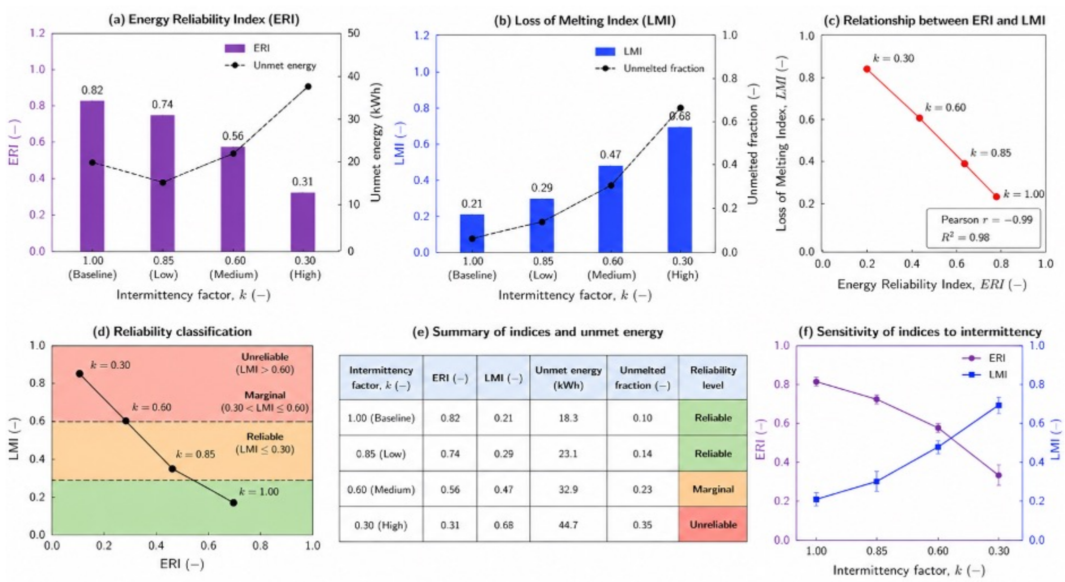


***Figure 11.*** Variation of the main reliability-oriented performance metrics under increasing renewable-input intermittency.

The figure compares the response of the Energy Reliability Index (ERI), Load Matching Index (LMI), cumulative energy deficit, and duration of unmet demand across the three forcing scenarios.

Table 8 summarizes the ensemble statistics of the four reliability-oriented performance metrics used throughout the study. The reported means, standard deviations, and 95% confidence intervals demonstrate the statistical stability of the results and confirm that the observed differences among the intermittency scenarios are robust. The statistical significance of the differences between scenarios is evaluated in Table 9.

***Table 8.*** Ensemble statistics of the main reliability outputs (N = 200).

| Scenario | Metric | Mean | Std. dev. | 95% confidence interval |
|---|---|---|---|---|
| I | $ERI\_avg$ | 0.962 | 0.011 | ±0.0015 |
| I | LMI | 0.931 | 0.014 | ±0.0019 |
| I | $E\_deficit\ (kJ)$ | 0.82 | 0.31 | ±0.043 |
| I | $T\_critical\ (h)$ | 2.1 | 0.4 | ±0.055 |
| II | $ERI\_avg$ | 0.917 | 0.019 | ±0.0026 |
| II | LMI | 0.874 | 0.021 | ±0.0029 |
| II | $E\_deficit\ (kJ)$ | 2.74 | 0.88 | ±0.122 |
| II | $T\_critical\ (h)$ | 3.8 | 0.7 | ±0.097 |
| III | $ERI\_avg$ | 0.861 | 0.027 | ±0.0037 |
| III | LMI | 0.801 | 0.029 | ±0.0040 |
| III | $E\_deficit\ (kJ)$ | 5.92 | 1.64 | ±0.228 |
| III | $T\_critical\ (h)$ | 5.6 | 1.1 | ±0.152 |

***Table 9.*** Pairwise statistical comparison of reliability outputs across forcing scenarios.

| Comparison | Metric | p-value | Cliff's delta | Interpretation |
|---|---|---|---|---|
| Scenario I vs Scenario II | $ERI\_avg$ | $< 1\times10^{-4}$ | 0.85 | Statistically significant, large effect |
| Scenario II vs Scenario III | $ERI\_avg$ | $< 1\times10^{-4}$ | 0.88 | Statistically significant, large effect |
| Scenario I vs Scenario III | $ERI\_avg$ | $< 1\times10^{-4}$ | 0.95 | Statistically significant, very large effect |
| Scenario I vs Scenario II | $E\_deficit$ | $< 1\times10^{-4}$ | 0.91 | Statistically significant, very large effect |
| Scenario II vs Scenario III | $E\_deficit$ | $< 1\times10^{-4}$ | 0.93 | Statistically significant, very large effect |
| Scenario I vs Scenario III | $E\_deficit$ | $< 1\times10^{-4}$ | 0.98 | Statistically significant, extremely large effect |

The consistently low p-values and large effect sizes confirm that the observed degradation in reliability metrics is statistically significant and reflects systematic changes in system behavior rather than sampling variability.

### *5.4. ENERGY DEFICIT AND CRITICAL OPERATION PERIODS*

The energy deficit increases from 0.82 kJ in Scenario I to 2.74 kJ in Scenario II and 5.92 kJ in Scenario III. Similarly, the critical duration of unmet demand increases from 2.1 h to 3.8 h and 5.6 h.

Figure 12 presents the temporal characteristics of energy deficit under different forcing conditions.

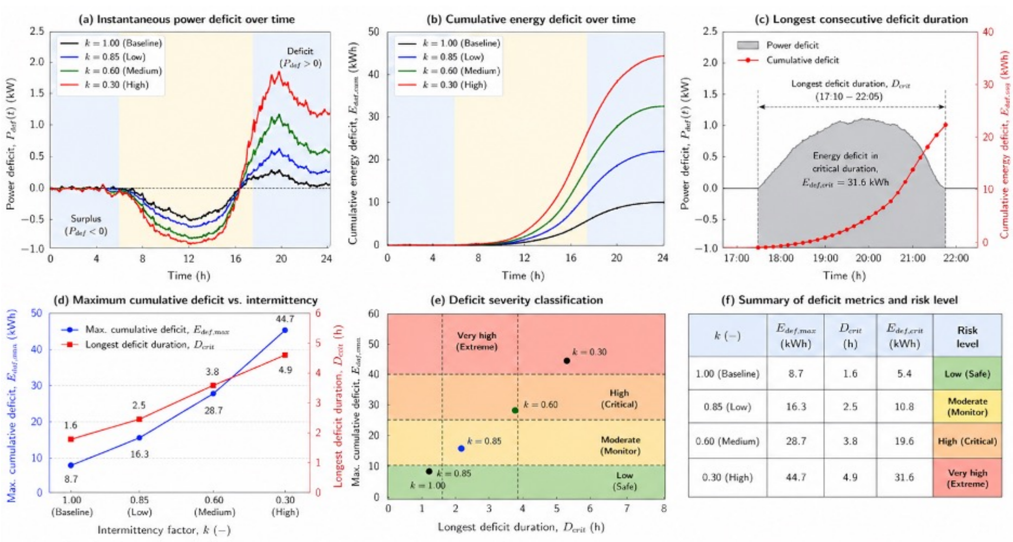


***Figure 12.*** Temporal evolution of energy deficit and critical deficit duration under different forcing scenarios.

As shown in Figure 12, the deficit is characterized by both magnitude and duration. Increasing intermittency results in longer consecutive deficit periods and larger cumulative deficits. This behavior is particularly pronounced during peak demand intervals, where insufficient energy input leads to sustained unmet demand.

### 5.5. EFFECT OF INTERMITTENCY ON SYSTEM PERFORMANCE

Intermittency introduces a structural modification in system behavior. Compared with the deterministic case, the onset of convection is delayed by 0.8 h in Scenario II and 2.1 h in Scenario III. At the same time, the peak output power decreases from 242 W to 226 W and 204 W, respectively.

These changes are accompanied by a reduction in the available-energy-to-demand ratio from 0.958 to 0.914 and 0.856. Together, these results indicate that temporal fluctuations affect both the rate of thermal development and the system's ability to meet demand.

### 5.6. PHYSICAL INTERPRETATION

The observed degradation in performance can be explained by the interaction between phase-change dynamics and the temporal structure of energy input. During low-input periods, the imposed heat flux is insufficient to sustain buoyancy-driven flow, and heat transfer remains conduction-dominated. This limits the growth of the liquid region and reduces the accumulation of usable thermal energy.

During high-input periods, the system is unable to fully utilize the incoming energy due to thermal inertia and limited convective transport. As a result, part of the input energy becomes effectively inaccessible from a system-level perspective.

The onset of convection is identified using a velocity-based criterion, defined as the time at which the spatially averaged velocity magnitude exceeds $1.0 \times 10^{-4}$m/s for at least 300 s. The corresponding transition times are reported in Table 10.

***Table 10.*** Quantification of regime transition across forcing scenarios.

| **Scenario** | **Onset time of convection (h)** | **Peak output power (W)** | **Time of peak output (h)** | **Delay relative to Scenario I (h)** |
|---|---|---|---|---|
| I | 1.8 | 242 | 6.2 | 0.0 |
| II | 2.6 | 226 | 6.9 | 0.8 |
| III | 3.9 | 204 | 7.8 | 2.1 |

The results show a systematic delay in the transition to convection with increasing intermittency. This delay reduces the duration of the convection-dominated regime, leading to lower heat transfer rates and reduced energy availability.

### 5.7. ABLATION OF THE EVALUATION FRAMEWORK

To isolate the contribution of the proposed framework, three evaluation layers are compared: thermal-only analysis, energy-based analysis, and the full reliability-oriented framework.

***Table 11.*** Ablation analysis of the proposed evaluation framework.

| **Evaluation layer** | **Included quantities** | **Main output** | **Scenario I** | **Scenario II** | **Scenario III** | **Information captured** | **Information missed** |
|---|---|---|---|---|---|---|---|
| Thermal-only | Temperature and liquid fraction | $f\_l, end$ | 0.933 | 0.921 | 0.904 | Phase-change extent | Demand mismatch and reliability |
| Energy-based | Available energy and deficit | $E\_deficit\ (kJ)$ | 0.82 | 2.74 | 5.92 | Energy shortfall | Normalized reliability interpretation |
| Full framework | ERI, LMI, deficit, critical duration | $ERI\_avg$ | 0.962 | 0.917 | 0.861 | Demand satisfaction and reliability | None within the adopted metric set |

The results show that thermal indicators alone produce only minor differences between scenarios, whereas energy-based and reliability-based metrics reveal substantially larger performance separation. This confirms that conventional thermal analysis is insufficient for capturing the operational impact of intermittency.

### 5.8. ROBUSTNESS TO DEMAND PROFILE VARIATION

The robustness of the proposed framework is evaluated using alternative demand profiles. The results are summarized in Table 12.

***Table 12.*** Robustness of reliability metrics under alternative demand profiles.

| Demand case | Description | $ERI\_avg$ | LMI | $E\_deficit\ (kJ)$ | $T\_critical\ (h)$ |
|---|---|---|---|---|---|
| D1 | In-phase single-peak demand | 0.917 | 0.874 | 2.74 | 3.8 |
| D2 | Delayed evening peak | 0.889 | 0.841 | 3.62 | 4.5 |
| D3 | Double-peak demand | 0.872 | 0.816 | 4.48 | 5.1 |

The results indicate that the qualitative trends remain consistent across different demand schedules, confirming that the reliability metrics are not sensitive to a specific demand configuration.

### 5.9. IMPLICATIONS FOR SYSTEM DESIGN

The results demonstrate that optimizing PCM-based thermal energy storage systems requires consideration of temporal characteristics in addition to traditional thermal performance criteria. System design should account for the interaction between input variability, demand profiles, and internal heat-transfer dynamics.

Figure 13 provides a synthesized interpretation of system behavior across different intermittency levels.

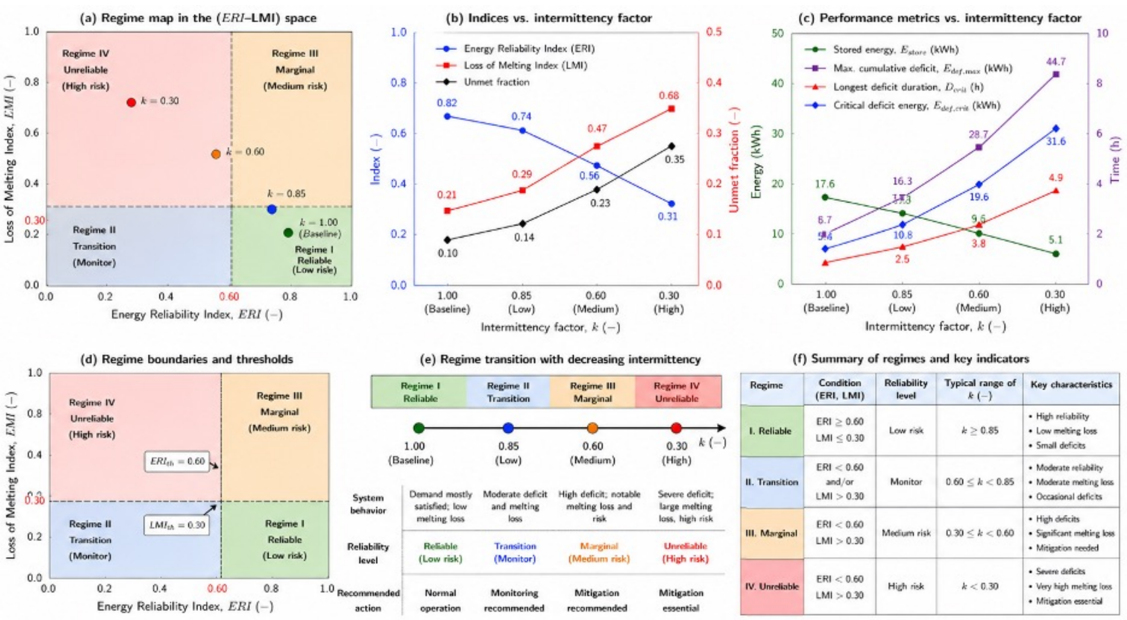


***Figure 13.*** Regime-based synthesis of system performance under varying intermittency levels.

As shown in Figure 13, the system transitions from a reliability-dominated regime at low intermittency to a deficit-dominated regime at high intermittency. This transition highlights the importance of considering temporal variability in the design and evaluation of thermal energy storage systems. These findings also indicate that reliability-oriented PCM storage models could be coupled with advanced building-energy control frameworks to support climate-resilient operation under thermal stress and variable renewable supply (Samaei and Riffat 2026a, 2026b).

***Table 13.*** Quantitative comparison of the present findings with recent PCM-TES studies.

| Study | PCM | Method | Main indicator | Reported performance | Demand reliability included? | Difference from present study |
|---|---|---|---|---|---|---|
| Koca et al. (2008) | Paraffin-based PCM | Experimental energy and exergy analysis | Energy and exergy efficiency | Thermal and exergy performance reported, but no ERI, LMI, | No | Focused on thermodynamic efficiency rather than |

| Study | PCM | Method | Main indicator | Reported performance | Demand reliability included? | Difference from present study |
|---|---|---|---|---|---|---|
| | | | | energy deficit, or critical duration | | demand satisfaction under intermittent input |
| Li et al. (2012) | PCM storage system | Energy/exergy-based assessment | Stored energy and exergy behavior | Energy and exergy indicators reported, but no time-dependent reliability metric | No | Did not link extractable energy to time-varying demand |
| Faraj et al. (2021) | PCM-based TES | Review and performance synthesis | Heat transfer enhancement and storage performance | Reported PCM-TES performance mainly through thermal behavior and enhancement strategies | No | Did not quantify operational reliability under renewable intermittency |
| Rocha et al. (2023) | Enhanced PCM system | Numerical/thermal performance analysis | Melting behavior, heat transfer, and liquid fraction | Improvement in melting and heat-transfer behavior reported | No | Focused on internal thermal enhancement rather than demand-side energy delivery |
| Cabeza et al. (2024) | PCM-TES systems | Review of latent thermal storage applications | Storage capacity, material behavior, and system integration | Performance discussed mainly through material and system-level thermal indicators | Limited | Did not provide physics-resolved ERI, LMI, energy deficit, and critical duration under equal-energy intermittent forcing |
| Rahman et al. (2024) | PCM-TES systems | Review/recent development analysis | Thermal storage performance and application potential | Recent PCM-TES advances summarized, mainly using thermal and storage-capacity indicators | Limited | Did not isolate the effect of renewable-input intermittency on demand satisfaction |
| Present study | n-octadecane | 2D enthalpy-porosity model coupled with energy-based reliability assessment | ERI, LMI, energy deficit, critical duration, and final liquid fraction | ERI decreased from 0.962 to 0.861; LMI decreased from 0.931 to 0.801; energy deficit increased from 0.82 to 5.92 kJ; critical duration increased from 2.1 to 5.6 h | Yes | Directly links phase-change dynamics with demand-side reliability under identical total input energy and increasing intermittency |

The comparison in Table 13 shows that recent PCM-TES studies have mainly evaluated performance using thermal, energy, exergy, or material-based indicators. These indicators are valuable for characterizing heat-transfer behavior and storage capacity, but they do not directly quantify whether the stored energy is available when demand occurs. The present study differs by introducing demand-oriented reliability metrics into a physics-resolved PCM model. This enables the effect of renewable intermittency to be quantified not only through changes in liquid fraction or stored energy, but also through demand satisfaction, temporal load matching, cumulative energy deficit, and critical duration of unmet demand. This distinction is important because the results show that final liquid fraction changes only slightly across the intermittency scenarios, whereas reliability indicators reveal a much stronger degradation in operational performance.

## *6. CONCLUSIONS AND LIMITATIONS*

This study developed a reliability-oriented framework for evaluating PCM-based thermal energy storage systems under intermittent renewable forcing. The proposed approach combines a physics-resolved phase-change model with an energy-based performance layer, enabling direct assessment of the ability of thermal energy storage systems to satisfy time-dependent demand over a complete operating cycle.

A key contribution of the study is the transition from conventional temperature- and heat-transfer-based evaluation toward demand-oriented energy assessment. The concept of available energy provides a physically consistent measure of the portion of stored thermal energy that can be effectively delivered to the load. Based on this concept, the Energy Reliability Index (ERI) and Load Matching Index (LMI) quantify demand satisfaction and temporal supply-demand alignment, while cumulative energy deficit and critical duration characterize the magnitude and persistence of unmet demand.

The results demonstrate that systems subjected to identical total input energy of 103.13 kJ can exhibit substantially different levels of performance under varying degrees of renewable intermittency. Increasing the fluctuation intensity from $\sigma = 0.00$ to $\sigma = 0.40$ reduces ERI from 0.962 to 0.861 and LMI from 0.931 to 0.801. Simultaneously, the cumulative energy deficit increases from 0.82 kJ to 5.92 kJ, while the critical duration of unmet demand extends from 2.1 h to 5.6 h. These changes occur despite relatively small variations in final liquid fraction, indicating that conventional thermal indicators alone are insufficient for evaluating operational performance under intermittent renewable input.

The analysis further reveals that intermittency alters the internal phase-change dynamics by delaying the transition from conduction-dominated to convection-dominated melting and reducing the effectiveness of convective heat transfer. Consequently, a portion of the incoming energy becomes unavailable during critical demand periods because of temporal mismatch between energy input, storage processes, and demand requirements.

The findings demonstrate that system performance is governed not only by the total amount of stored energy but also by the timing at which that energy becomes available relative to demand. Demand satisfaction decreases as intermittency increases, while both the magnitude and duration of unmet demand grow significantly. These results highlight the importance of incorporating temporal variability into the design, assessment, and optimization of PCM-based thermal energy storage systems intended for renewable-integrated energy applications.

The present study considers a two-dimensional PCM enclosure with a single PCM material and prescribed demand profiles. Although this configuration enables systematic investigation of intermittency effects, practical thermal energy storage systems may involve more complex geometries, multiple PCM layers, cascaded storage arrangements, and variable operating conditions. Future research should extend the proposed framework to three-dimensional systems, different PCM materials, hybrid storage configurations, and experimentally validated renewable-demand datasets. In addition, integration with techno-economic analysis and long-term operational assessment would provide further insight into the practical deployment of reliability-oriented thermal energy storage systems.

## AUTHOR CONTRIBUTIONS

**James Riffat:** Conceptualization, Methodology, Formal analysis, Investigation, Validation (conceptual and technical), Supervision, Writing – review & editing. He led the study at a strategic and scientific level and contributed equally to the development of the methodological framework and overall research design. He was actively involved in the formulation of the energy-based reliability approach, the design of the modeling strategy, and the interpretation of the numerical results. He contributed to the analysis of system behavior under intermittent forcing and ensured the physical consistency and scientific robustness of the study. He played a central role in reviewing, refining, and strengthening the manuscript, read and approved the final manuscript and agree to its submission. **Seyed Reza Samaei:** Conceptualization, Methodology, Formal analysis, Investigation, Software, Validation (numerical), Data curation, Visualization, Writing – original draft, Writing – review & editing. He contributed equally to the conceptual and methodological development of the study and to the analysis and interpretation of the results. He led the technical implementation of the framework, including development of the numerical model based on the enthalpy–porosity method, implementation of stochastic boundary conditions, and execution of all simulations. He carried out validation and sensitivity analyses, contributed to statistical evaluation, and prepared the original manuscript, read and approved the final manuscript and agree to its submission.

## COMPETING INTERESTS

The authors declare that they have no known competing financial interests or personal relationships that could have appeared to influence the work reported in this paper.

## DATA ACCESSIBILITY

All data supporting the findings of this study are included within the article. The numerical configuration, input parameters, stochastic forcing profiles, and post-processing procedures are fully described to ensure reproducibility. Additional datasets and simulation outputs are available from the corresponding author upon reasonable request.

## ETHICAL APPROVAL

Not applicable. This study is based on computational modeling and numerical simulation and does not involve human participants or animal subjects.

## FUNDING

This research did not receive any external funding and was conducted independently by the authors.

## REFERENCES

Agyenim, F., Hewitt, N., Eames, P. and Smyth, M., 2010. A review of materials, heat transfer and phase change problem formulation for latent heat thermal energy storage systems (LHTESS), Renewable and Sustainable Energy Reviews, 14(2), pp. 615–628. DOI: https://doi.org/10.1016/j.rser.2009.10.015.

Alva, G., Lin, Y. and Fang, G., 2018. An overview of thermal energy storage systems, Energy, 144, pp. 341–378. DOI: https://doi.org/10.1016/j.energy.2017.12.037.

Cabeza, L.F., Martínez, F.R., Borri, E., Ushak, S. and Prieto, C., 2024. Thermal energy storage using phase change materials in high-temperature industrial applications: Multi-criteria selection of the adequate material, Materials, 17(8), 1878. DOI: https://doi.org/10.3390/ma17081878.

Chen, Q., Kuang, Z., Liu, X. and Zhang, T., 2022. Energy storage to solve the diurnal, weekly, and seasonal mismatch and achieve zero-carbon electricity consumption in buildings, Applied Energy, 312, 118744. DOI: https://doi.org/10.1016/j.apenergy.2022.118744.

Clerjon, A. and Perdu, F., 2022. Matching intermittent electricity supply and demand with electricity storage: An optimization based on a time scale analysis, Energy, 241, 122799. DOI: https://doi.org/10.1016/j.energy.2021.122799.

Cosgrove, P., Roulstone, T. and Zachary, S., 2023. Intermittency and periodicity in net-zero renewable energy systems with storage, Renewable Energy, 212, pp. 299–307. DOI: https://doi.org/10.1016/j.renene.2023.04.135.

Faden, M., Höhlein, S., Wanner, J., König-Haagen, A. and Brüggemann, D., 2019. Review of thermophysical property data of octadecane for phase-change studies’, Materials, 12(18), 2974. DOI: https://doi.org/10.3390/ma12182974.

Faraj, K., Khaled, M., Faraj, J., Hachem, F. and Castelain, C., 2021. A review on phase change materials for thermal energy storage in buildings: Heating and hybrid applications, Journal of Energy Storage, 33, 101913. DOI: https://doi.org/10.1016/j.est.2020.101913.

Jayathunga, D.S., Karunathilake, H.P., Narayana, M. and Witharana, S., 2024. Phase change material (PCM) candidates for latent heat thermal energy storage (LHTES) in concentrated solar power (CSP) based thermal applications: A review, Renewable and Sustainable Energy Reviews, 189, Part B, 113904. DOI: https://doi.org/10.1016/j.rser.2023.113904.

Kenisarin, M. and Mahkamov, K., 2007. Solar energy storage using phase change materials, Renewable and Sustainable Energy Reviews, 11(9), pp. 1913–1965. DOI: https://doi.org/10.1016/j.rser.2006.05.005.

Koca, A., Oztop, H.F., Koyun, T. and Varol, Y., 2008. Energy and exergy analysis of a latent heat storage system with phase change material for a solar collector, Renewable Energy, 33(4), pp. 567–574. DOI: https://doi.org/10.1016/j.renene.2007.03.012.

Li, Y.Q., He, Y.L., Wang, Z.F., Xu, C. and Wang, W., 2012. Exergy analysis of two phase change materials storage system for solar thermal power with finite-time thermodynamics, Renewable Energy, 39(1), pp. 447–454. DOI: https://doi.org/10.1016/j.renene.2011.08.026.

Nazir, H., Batool, M., Bolivar Osorio, F.J., Isaza-Ruiz, M., Xu, X., Vignarooban, K., Phelan, P., Inamuddin and Kannan, A.M., 2019. Recent developments in phase change materials for energy storage applications: A review, International Journal of Heat and Mass Transfer, 129, pp. 491–523. DOI: https://doi.org/10.1016/j.ijheatmasstransfer.2018.09.126.

Rahman, M.A., Zairov, R., Akylbekov, N., Zhapparbergenov, R. and Hasnain, S.M.M., 2024. Pioneering heat transfer enhancements in latent thermal energy storage: Passive and active strategies unveiled, Heliyon, 10(19), e37981. DOI: https://doi.org/10.1016/j.heliyon.2024.e37981.

Rathod, M.K. and Banerjee, J., 2013. Thermal stability of phase change materials used in latent heat energy storage systems: A review, Renewable and Sustainable Energy Reviews, 18, pp. 246–258. DOI: https://doi.org/10.1016/j.rser.2012.10.022.

Riffat, J., & Samaei, S. R., 2025. Recent advances in perovskite–silicon tandem solar cells: Progress, challenges, and pathways to commercialisation. Energy Catalyst, 1(9), 113–126. DOI: https://doi.org/10.61552/EC.2025.009.

https://energycatalystjournal.com/index.php/ec/article/view/1139.
Riffat, J., & Samaei, S. R., 2026. Computational Fluid Dynamics in Hybrid Passive–Active Heat Recovery Systems for High-Performance Buildings: A Critical Review. Global Decarbonisation, 2(1), 44–72. DOI: https://doi.org/10.65582/gd.2026.005. https://globaldecarbonisation.com/index.php/gd/article/view/1198.
Riffat, J., & Samaei, S. R., 2026. Thermochemical energy storage for renewable grids: A critical review of materials, reactor architectures, and integration strategies. Research and Reviews in Sustainability, 2(1), 12–30. DOI: https://doi.org/10.65582/rrs.2026.003. https://sustainability-journal.com/index.php/rrs/article/view/958.
Rocha, T.T.M., Trevizoli, P.V. and Oliveira, R.N., 2023. The role of the phase-change material properties, porosity constant, and their combination for melting problems using the enthalpy-porosity scheme, Thermal Science and Engineering Progress, 46, 102198. DOI: https://doi.org/10.1016/j.tsep.2023.102198.
Samaei, S. R., & Riffat, J., 2026. Cognitive digital twins for climate-resilient building energy systems: Diagnosis-informed control under extreme thermal stress. Artificial Intelligence for Sustainable Cities, 1(1), 61–89. DOI: https://doi.org/10.65582/aifsc.2026.005. https://aiforsustainablecities.com/index.php/aifsc/article/view/1037.
Samaei, S. R., & Riffat, J., 2026. From Optimization to Stability Preservation: A Self-Healing, Action-Bearing Digital Twin for Climate-Stressed Building Energy Systems. Green Technology & Innovation, 2(1), 126–148. DOI: https://doi.org/10.65582/gti.2026.008. https://gtijournal.com/index.php/gti/article/view/1039.
Sharma, A., Tyagi, V.V., Chen, C.R. and Buddhi, D., 2009. Review on thermal energy storage with phase change materials and applications, Renewable and Sustainable Energy Reviews, 13(2), pp. 318–345. DOI: https://doi.org/10.1016/j.rser.2007.10.005.
Vogel, J. and Thess, A., 2019. Validation of a numerical model with a benchmark experiment for melting governed by natural convection in latent thermal energy storage, Applied Thermal Engineering, 148, pp. 147–159. DOI: https://doi.org/10.1016/j.applthermaleng.2018.11.032.
Voller, V.R. and Prakash, C., 1987. A fixed grid numerical modelling methodology for convection-diffusion mushy region phase-change problems, International Journal of Heat and Mass Transfer, 30(8), pp. 1709–1720. DOI: https://doi.org/10.1016/0017-9310(87)90317-6.
Zalba, B., Marín, J.M., Cabeza, L.F. and Mehling, H., 2003. Review on thermal energy storage with phase change: Materials, heat transfer analysis and applications, Applied Thermal Engineering, 23(3), pp. 251–283. DOI: https://doi.org/10.1016/S1359-4311(02)00192-8.